Journal of
Materials Chemistry A

Materials for energy and sustainability

rsc.li/materials-a

ROYAL SOCIETY OF CHEMISTRY
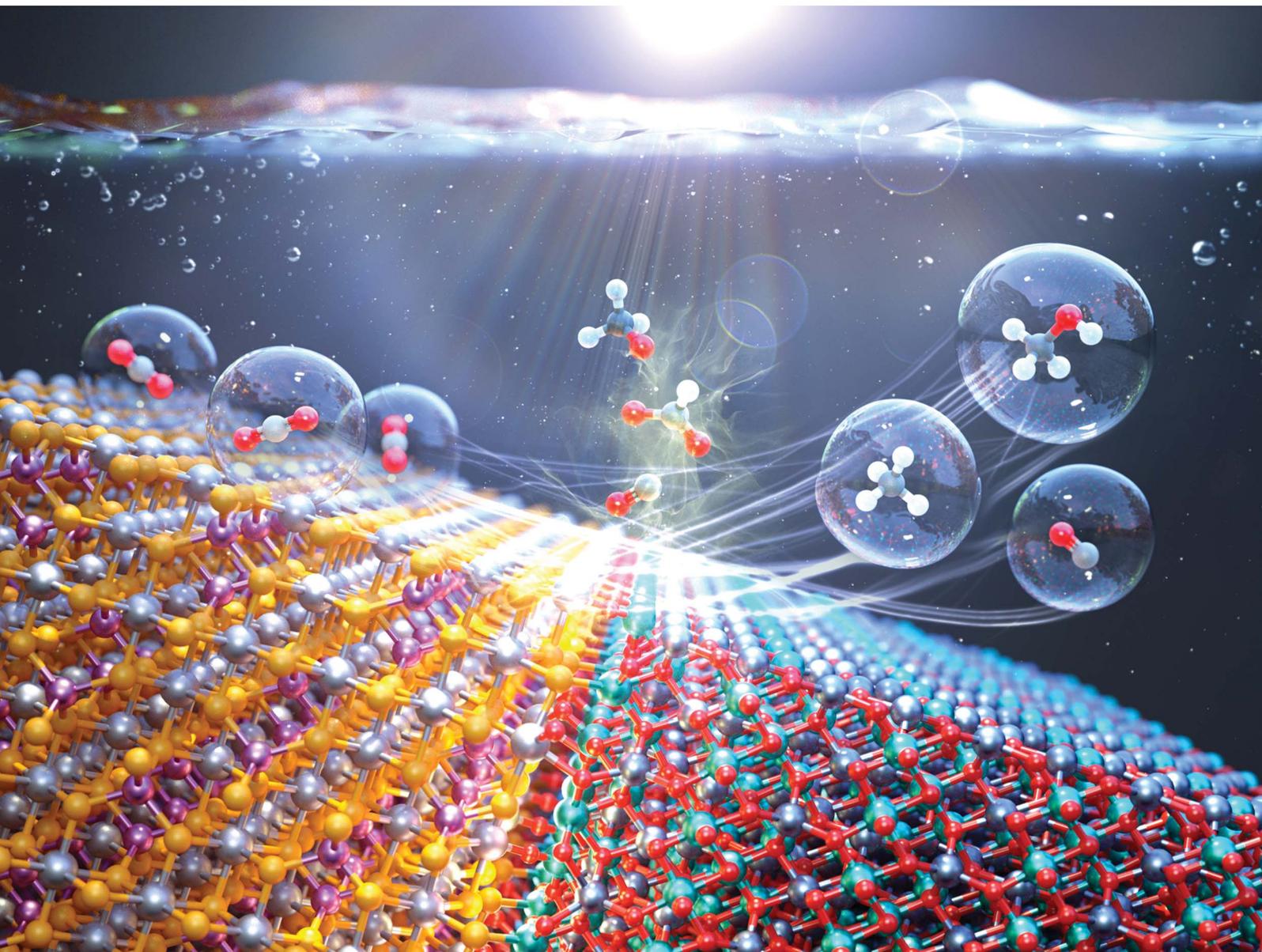
PAPER
Xiaofang Jia, Caroline Sunyong Lee *et al.*
Enhanced interfacial charge separation *via* $MnIn_2S_4/Zn_2TiO_4$ heterojunction for light-induced fuel production

ROYAL SOCIETY
OF CHEMISTRY

PAPER

Check for updates

Enhanced interfacial charge separation *via* MnIn$_2$S$_4$/Zn$_2$TiO$_4$ heterojunction for light-induced fuel production

Plassidius J. Chengula,[a] Junying Zhang, [ID][b] Hazina Charles,[a] Ji Yeon Seo,[a] Xiaofang Jia [ID]*[c] and Caroline Sunyong Lee [ID]*[a]

Sustainable development necessitates photocatalytic CO_2 reduction for generating value-added carbon products. However, synthesizing photocatalysts with superior carrier-separation capabilities *via* straightforward methods for the photoreduction of CO_2 remains a significant challenge. In this study, we present a unique interfacial-heterostructured photocatalyst synthesized through the *in situ* growth of $MnIn_2S_4$ (MIS) nanosheets on Zn_2TiO_4 (ZTO) nanorods constructed from several zinc glycolates *via* a sol−gel process. The active sites of MIS facilitated the conversion of CO_2 into formate and promoted the desorption of CO* from its surface, producing value-added carbon products as confirmed by both *in situ* experimental characterization and theoretical calculations. Compared with the other samples, the optimal photocatalyst (0.4-MIS/ZTO) exhibited exceptional activity for CO_2 photoreduction under ultraviolet-visible light irradiation, with CO, CH_4, and CH_3OH gas yields of 484, 345, and 4457 μmol g^{-1} within 7 h, respectively. The exceptional photocatalytic activity of 0.4-MIS/ZTO can be attributed to the effective modification of the surface and S-scheme interface of the heterostructure, promoting charge-pair generation, separation, and transfer. This study presents a simple and efficient strategy for constructing high-performance 2D/1D heterostructures to convert CO_2 into high-value carbon products through photocatalytic reduction.

1 Introduction

Growing concerns regarding global warming and energy security have intensified research into sustainable methods for reducing carbon dioxide (CO_2).[1–4] The conversion of CO_2 into valuable chemicals such as methanol (CH_3OH) is a promising strategy for mitigating CO_2 emissions while producing clean fuels. CH_3OH is attractive because it serves as a renewable fuel and essential feedstock in the chemical industry.[5,6] Semiconductor photocatalysis plays a vital role in addressing contemporary energy and environmental challenges.[7,8] Although TiO_2 is a widely recognized and extensively used photocatalytic material given its stability and affordability, its wide bandgap limits its ability to harness solar energy, thereby restricting its use to a small ultraviolet (UV) fraction (3–5%).[9–11] Therefore, the development of novel and effective photocatalysts sensitive to visible light remains a critical and challenging task.

Nanoscience offers significant potential for advancing photocatalysts by providing strategies to design and control their properties, including energy gaps, chemical composition, and surface characteristics. For example, variations in particle size and shape significantly affect photocatalytic performance, prompting the synthesis of nanostructures with diverse morphologies to understand their photocatalytic behavior.[12,13] Inorganic nanorods such as Zn_2TiO_4 (ZTO) are promising because of their distinctive properties such as abundant defect sites from cation disorder and oxygen vacancies, which enables efficient charge separation and facilitates strong interfacial coupling when forming heterojunctions.[14,15] However, they are often scarce, particularly for materials with complex or oxide-based structures. In many synthetic processes, nanorod formation competes with nanoparticle formation. Despite meeting all prerequisites and progressing through the expected intermediates of nanorod synthesis, the final product can still contain nanoparticles.[16–19] Consequently, relinquishing the complex objective of synthesizing anisotropic nanostructures enables a broader range of synthetic pathways, fabricating nanobelts, nanowires, and hierarchical nanostructures with nearly any desired dimension.

ZTO is a conventional A$_2$BO$_4$ layered perovskite oxide that exhibits a tetragonal or orthorhombic structure when half the A-site cations are substituted with B-site cations. Although ZTO

[a]Department of Materials and Chemical Engineering, Hanyang University, Gyeonggi-do, 426-791, Korea. E-mail: sunyonglee@hanyang.ac.kr

[b]School of Physics, Beihang University, Beijing 100191, China. E-mail: zjy@buaa.edu.cn

[c]School of Physical Science and Technology, Inner Mongolia University, Hohhot 010021, China. E-mail: jiaxiaofang@imu.edu.cn

This journal is © The Royal Society of Chemistry 2026

J. Mater. Chem. A, 2026, **14**, 16409–16423 | **16409**

has been explored for catalytic applications, its photochemical properties have received limited attention because it functions as a wide-bandgap semiconductor with a bandgap of 3.11 eV.[20–22] The conduction band (CB) of ZTO is more negative than the redox potential of H^+/H_2 (0 V vs. normal hydrogen electrode (NHE)), whereas its valence band (VB) is more positive than the redox potential of O_2/H_2O (1.23 eV).[23] However, reports on its band structure confirm that the CB of ZTO is not sufficiently negative to generate H_2, while its VB is sufficiently positive to generate O_2 radicals, making it a promising photocatalyst for CO_2 reduction and the photooxidation of volatile organic compounds.

Thus far, several ZTO-based heterostructures, including TiO_2/ZTO, ZnO/ZTO, ZnS/ZTO, and $ZnIn_2S_4$/ZTO, have been successfully synthesized, demonstrating improved charge separation and photocatalytic performance under visible light irradiation.[24–27] Mn-based photocatalysts have gained considerable attention because of their potential for various photocatalytic applications. $MnIn_2S_4$ (MIS) is a ternary chalcogenide from the AB_2S_4 family (A = Mn and B=In) that exhibits unique magnetic, electronic, and optical properties with a strong visible-light response (E_g = 1.8–2.5 eV) by covering ∼43% of the solar spectrum.[28,29] These characteristics make MIS an excellent alternative to construct heterojunctions with wide-bandgap materials for enhancing charge separation and visible-light absorption. To the best of our knowledge, MIS/ZTO heterostructures have been synthesized for the first time in this study, demonstrating superior photocatalytic performance under UV-visible (UV-vis) light irradiation compared to their individual semiconductor components.

In this study, we synthesized MIS nanosheets on the surfaces of ZTO nanorods via a low temperature solvothermal reaction. This strategic design provides large specific surface areas and abundant active sites for photocatalytic reactions while effectively suppressing the recombination of photogenerated electrons and holes. Consequently, the optimized MIS/ZTO heterojunction exhibited superior photocatalytic performance, with total CO_2 conversion rates (including the combined yield of CO, CH_3OH, and CH_4) significantly higher than those obtained using pristine MIS and ZTO. In situ diffuse reflectance infrared Fourier transform spectroscopy (DRIFTS) and density functional theory (DFT) confirmed that MIS serves as a pivotal site in heterostructures, fostering the adsorption and desorption of the intermediate for methanol production. We comprehensively analyzed and discussed mechanisms underlying the enhanced photocatalytic performance of the MIS/ZTO heterostructure.

2 Experimental

2.1 Materials

All materials used in this study were of analytical grade and used as received. The photocatalysts were synthesized using ethylene glycol (EG) at an ambient temperature. Zinc(II) acetate dihydrate (Zn $(Ac)_2 \cdot 2H_2O$, purity ≥99%, Sigma-Aldrich) and titanium butoxide (Ti$(C_4H_9O)_4$, purity ≥97.0%, Sigma-Aldrich) were used as metal precursors, while EG (($C_2H_6O_2$), purity ≥99%, Sigma-Aldrich) served as the solvent and the reducing agent. Manganese chloride tetrahydrate ($MnCl_2 \cdot 4H_2O$, AR), indium chloride ($InCl_3$, AR), and thioacetamide (TAA, (C_2H_5NS), AR) are precursors of MIS.

2.2 Preparation of ZTO nanorods

In the conventional polyol process, the synthesis of ZTO involves dissolving Zn $(Ac)_2 \cdot 2H_2O$ in a polyol, typically at 30 °C or without heating, followed by the formation of an intermediate phase, nucleation, and subsequent growth. This ultimately leads to the formation of metal nanoparticles.

In this study, 0.5 mmol of Zn $(Ac)_2 \cdot 2H_2O$ is dissolved in 30 mL of EG, followed by the addition of 1.7 mL of Ti$(C_4H_9O)_4$, as shown in Fig. 1(a). The solution was stirred for 24 h, centrifuged to separate the solid and liquid phases, and washed twice with ethanol. After centrifugation, the samples were aged for 24 h and annealed at 600–700 °C for 2 h in air (heating rate = 5 °C min^{-1}) to produce ZTO nanorods with ilmenite and cubic structures. The prepared ZTO solution was white both before and after annealing.

2.3 Preparation of MIS/ZTO heterostructures

MIS nanosheets on ZTO nanorods were synthesized via a solvothermal method. The as-prepared ZTO nanorods (0.1 g) were dispersed in a mixture of 40 mL ethanol and 20 mL glycerol by ultrasonic treatment to form a uniform suspension. Next, $\times$ mmol $MnCl_2$, 2$\times$ mmol $InCl_3$, and 8$\times$ mmol TAA were dissolved in the suspension and stirred for 30 min (x = 0.1, 0.2, 0.4, or 0.6). The resulting mixture was transferred to a 100 mL Teflon-lined stainless-steel autoclave and heated at 120 °C for 3 h. The products were washed several times with water and ethanol, followed by vacuum drying at 60 °C for 12 h. The resulting yellowish powder was designated as x-MIS/ZTO; the sample with x = 0.1 was referred to as 0.1-MIS/ZTO. Finally, MIS microspheres were synthesized using the same procedure, except without the addition of ZTO, as shown in Fig. 1(b) and (c).

2.4 Photocatalyst characterization

X-ray diffraction (XRD) patterns of ZTO, MIS, and MIS/ZTO heterostructures were acquired using an X-ray diffractometer (D/Max-2500/PC; Cu/Kα source, λ = 1.5418 Å; Rigaku, Japan). The morphologies, elemental distributions, and microstructures of the samples were examined through high-resolution transmission electron microscopy (HR-TEM; JEM2100F, 200 kV, JEOL; Japan) and field-emission scanning electron microscopy (S4800, 15 kV; Hitachi, Japan). The optical absorption and bandgap were analyzed using UV-vis spectroscopy (V770; JASCO, Japan). The chemical states of the MIS/ZTO samples were investigated using X-ray photoelectron spectroscopy (XPS; K-Alpha⁺; Al/Kα source; Thermo Fisher Scientific, UK). Photoluminescence (PL; SC-100; Dongwoo, Korea) was used to assess charge recombination after He–Cd laser stimulation at 375 nm. The Mott–Schottky (M–S) method was used for determining the flat-band potentials (E_{fb}) using a three-electrode quartz setup submerged in 0.5 M Na_2SO_4 connected to a VersaSTAT 4 Potentiostat (Princeton Applied Research, USA) as described in SI (S1). The reference, counter, and working electrodes were Ag/
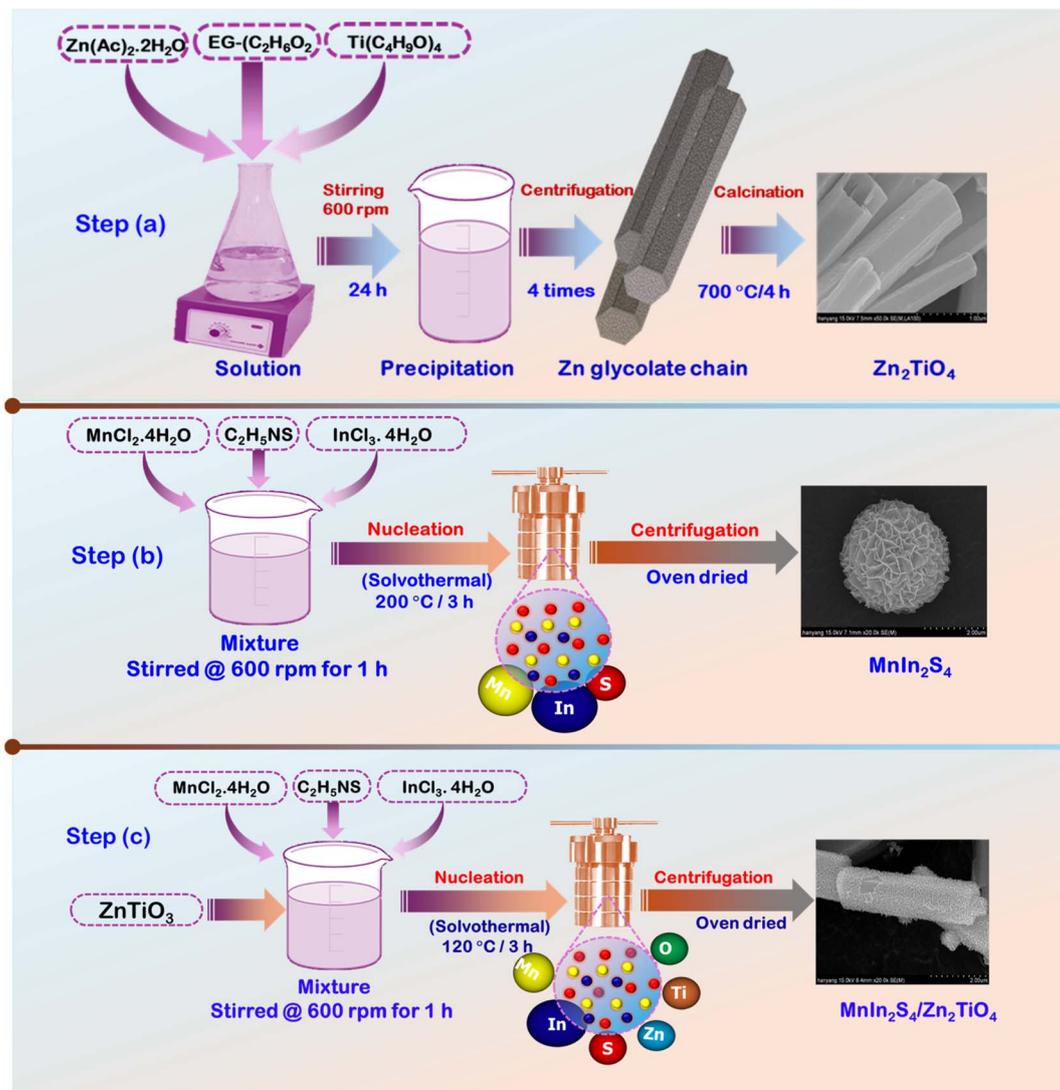
16410 | J. Mater. Chem. A, 2026, **14**, 16409–16423

This journal is © The Royal Society of Chemistry 2026

Fig. 1 Synthesis of (a) Zn_2TiO_4 (ZTO), (b) $MnIn_2S_4$ (MIS), and (c) MIS/ZTO heterostructures.

AgCl, Pt wire, and photoanode film, respectively. For sample preparation, 0.2 g MIS/ZTO was dispersed in 2 mL of ethanol. After complete dissolution, 0.5 mL of the solution was spin-coated onto an Fluorine doped Tin Oxide (FTO) glass (area = 10 cm^2) at 2500 rpm for 60 s. The coated films were dried in an oven for 2 h and sintered at 150 °C in air for 1 h to evaporate the ethanol. The samples were irradiated under UV-vis light, and the photoelectrochemical characteristics were evaluated.

2.5 DFT computations

The calculation was performed using DFT and the projection enhancement wave pseudo-pulse implemented in the Vienna *Ab initio* simulation package. The Perdew–Burke–Ernzerhof (PBE) of generalized gradient approximation was employed to describe the exchange and associated potentials.[30,31] In addition, the empirical correction method PBE + *D*3 (*D* stands for dispersion) was used to describe the van der Waals interaction.[32] The cut-off energy for the plane-wave basis was set to

450 eV. The Monkhorst–Pack $3 \times 3 \times 3$ grid for MIS and ZTO was selected in the first Brillouin zone. Structural relaxation stopped when the self-consistent total-energy difference and convergence criterion for forces on each atom were found to be less than 10^{-5} eV and 0.02 eV Å^{-1}, respectively. The interaction between adjacent plates was avoided by setting a vacuum region of 20 Å in the *z* direction. The free energy difference (ΔG) in the water redox reactions was calculated according to the approach proposed by Nørskov *et al.*[33] The formula at pH = 0 without solar irradiation can be defined as $\Delta G = \Delta E + \Delta E_{ZPE} - T\Delta S$, where ΔE, ΔE_{ZPE}, and ΔS represent the adsorption energy, difference in zero-point energy, and entropy difference between the adsorbed state and gas phase, respectively.

2.6 Photocatalytic CO_2 reduction

Photocatalytic CO_2 reduction experiments were conducted in a 250 mL custom-made quartz reactor as described in SI Section (S2). A mixture of distilled water (125 mL), photocatalysts with

This journal is © The Royal Society of Chemistry 2026

J. Mater. Chem. A, 2026, **14**, 16409–16423 | **16411**

varying compositions (2.0 mg), and triethanolamine (25 mL; TEOA; hole scavenger) was prepared. The reactor was sealed with a septum and positioned above an aqueous solution saturated with CO_2. The CO_2 gas was continuously purged for 2 h before the reaction. Gaseous products generated from CO_2 photoreduction were analyzed using gas chromatography (6500 GC; YL Instruments, Korea) equipped with a fused silica capillary column and pulsed discharge detector. Helium was used as the carrier gas. The photocatalytic reduction of CO_2 was conducted under UV-vis light irradiation using a 300 W Xe arc lamp (66984; Newport, USA).

3 Results and discussion

3.1 Photocatalyst morphology and structure

The morphologies of the ZTO, MIS, and 0.4-MIS/ZTO heterostructures were examined through SEM and TEM, as illustrated in Fig. 2 and S1. The SEM image of ZTO (Fig. 2(a)) reveals nanoscale particles with varying diameters, providing detailed morphological insights. Similarly, the SEM image of the MIS (Fig. 2(b)) shows that nanosheets are arranged in a stacked configuration. The SEM image of the 0.4-MIS/ZTO heterostructure (Fig. 2(c)) shows a uniform dispersion of MIS particles on the ZTO surface. In addition, the TEM analysis (Fig. 2(d) and (e)) confirmed a well-defined interface between ZTO and MIS. The HR-TEM image (Fig. 2(f)) shows distinct lattice fringes in the 0.4-MIS/ZTO structure with interplanar spacings of 0.3084 and 0.2542 nm corresponding to the (220) and (311) crystal

planes of MIS and ZTO, respectively. In addition, the TEM analysis indicated no visible interlayer gap between MIS and ZTO, suggesting the formation of intimate junctions between the two components.[34] Elemental distribution analysis using energy-dispersive X-ray spectroscopy (Fig. 2(g)) confirmed the presence of Zn, Ti, O, Mn, In, and S in the 0.4-MIS/ZTO heterostructure, thereby verifying the successful synthesis of the heterojunction structure.

3.2 XRD and selected area diffraction (SAED) patterns

Fig. 3(a) shows the powder XRD patterns of the ZTO, MIS, and MIS/ZTO heterostructures, which confirms their crystal structures. The sharp and well-defined diffraction peaks indicate high crystallinity. The diffraction peaks of ZTO appeared at $2\theta = 30.00°, 35.16°, 42.90°, 53.30°, 56.78°$, and $62.35°$ corresponding to the (220), (311), (400), (442), (511), and (440) crystal planes, respectively. These peaks are characteristic of the cubic crystal system (JCPDS card no. 025-1164).[26,35] Similarly, the MIS photocatalyst crystallized in the cubic phase, as confirmed by the JCPDS reference pattern (03-065-7474), exhibiting well-defined diffraction peaks at 14.1°, 23.3°, 27.4°, 33.3°, 43.7°, and 47.9°, which correspond to the (111), (220), (311), (400), (511), and (440) crystal planes, respectively.[28,29] The XRD patterns of the MIS/ZTO heterojunction structures revealed the simultaneous presence of MIS and ZTO phases. These patterns confirm the successful formation of the heterostructure. In addition, the intensity of the diffraction peak increased with an increase in
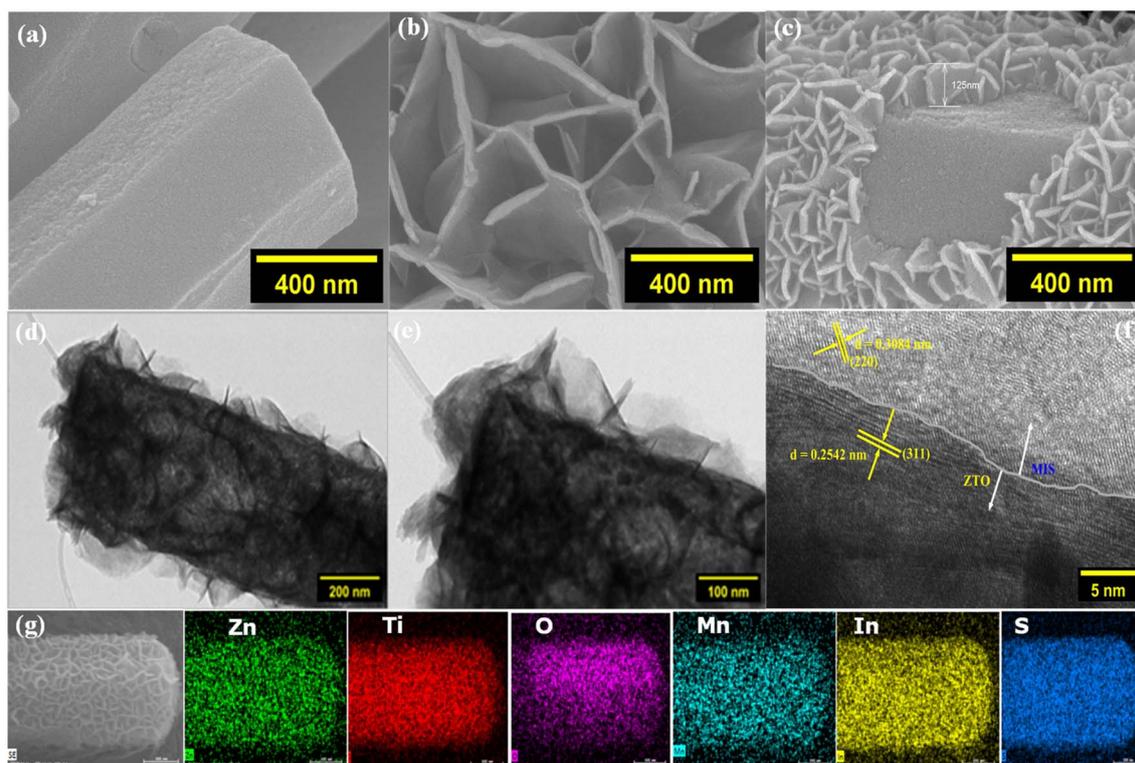

Fig. 2 SEM images of the (a) ZTO, (b) MIS, and (c) 0.4-MIS/ZTO heterostructures. (d and e) TEM images, (f) HR-TEM image, and (g) elemental mapping image obtained using energy-dispersive X-ray spectroscopy analysis of the 0.4-MIS/ZTO heterostructure.

16412 | *J. Mater. Chem. A*, 2026, **14**, 16409–16423

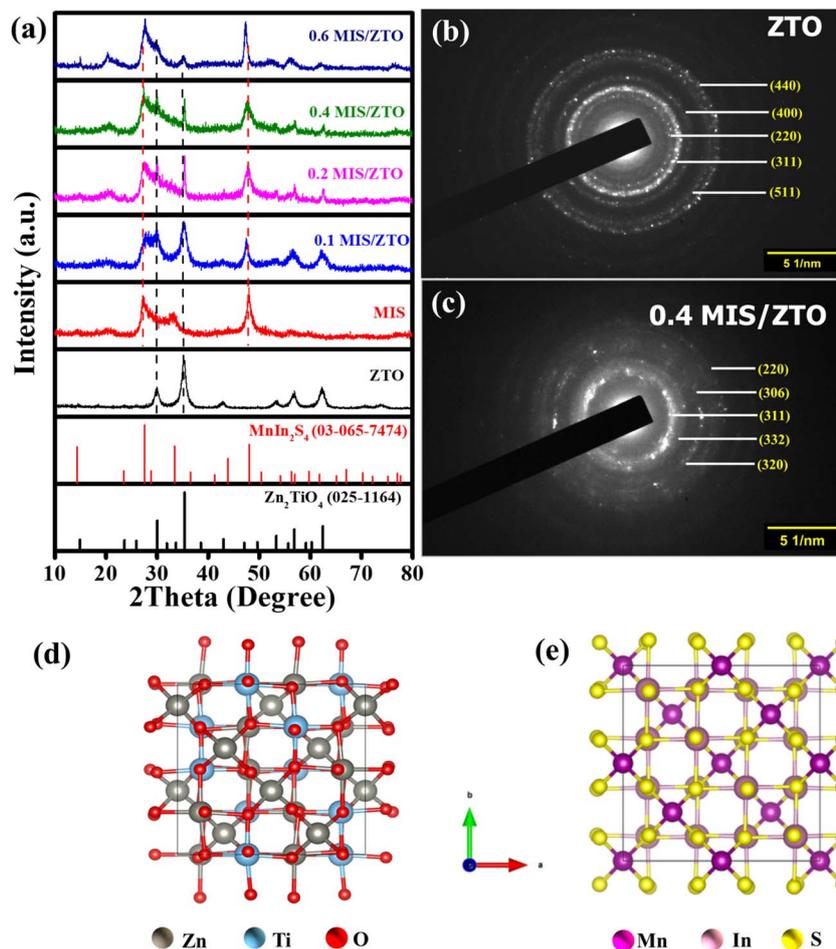This journal is © The Royal Society of Chemistry 2026

Fig. 3 (a) XRD patterns of the ZTO, MIS, and MIS/ZTO heterostructures. Selected area diffraction patterns of the (b) ZTO and (c) 0.4-MIS/ZTO heterostructure. Optimized crystal structures of (d) ZTO and (e) MIS.

ZTO content, while additional peaks corresponding to secondary phases or impurities were not detected. These findings validate the successful integration of MIS and ZTO into a well-defined heterojunction structure.

The selected area diffraction pattern in Fig. 3(b) shows bright diffraction rings corresponding to the (220), (311), (420), and (511) crystal lattice planes of cubic ZTO. Fig. 3(c) shows lattice spacings of 0.2535 and 0.3808 nm, which correspond to the (311) and (220) crystal planes of cubic ZTO and cubic MIS, respectively, in the 0.4-MIS/ZTO heterostructure. These results confirm that the hierarchical structure of polycrystalline MIS can be loaded successfully onto ZTO. Fig. 3(d) and (e) show that crystal structures illustrate the optimized configurations of ZTO and MIS.

3.3 Photoresponse and electronic structure evaluations

The interaction between ZTO and MIS in the MIS/ZTO heterostructures was investigated in addition to analyzing the morphological and structural properties of synthesized samples. The optical properties were assessed using UV-vis diffuse reflectance spectroscopy.

Fig. 4(a) shows that MIS and ZTO exhibit absorption edges at ~640 and 405 nm, respectively. The absorption edges of the composite samples (0.1-MIS/ZTO, 0.2-MIS/ZTO, 0.4-MIS/ZTO, and 0.6-MIS/ZTO) are positioned between those of the two pristine phases. The 0.4-MIS/ZTO sample exhibits neither an extended absorption edge nor an enhancement in light absorption intensity. Therefore, the effect of optical properties on photocatalytic improvement remains limited because the absorption range of the heterostructure remains confined between those of the individual components.[36] As illustrated in Fig. 4(b) using the Kubelka–Munk relationship, the estimated optical band gaps for MIS and ZTO are 1.94 and 3.06 eV, respectively. Therefore, optical results highlight the substantial impact of heterostructure engineering on the electronic properties of composites.

Decay lifetimes of the photogenerated charge carriers are evaluated using PL decay curves, as shown in Fig. 4(c). The average emission lifetimes of ZTO, MIS, and 0.4-MIS/ZTO heterostructures were determined by fitting the TR-PL spectra with a biexponential function and providing insights into their charge-transfer kinetics.

This journal is © The Royal Society of Chemistry 2026

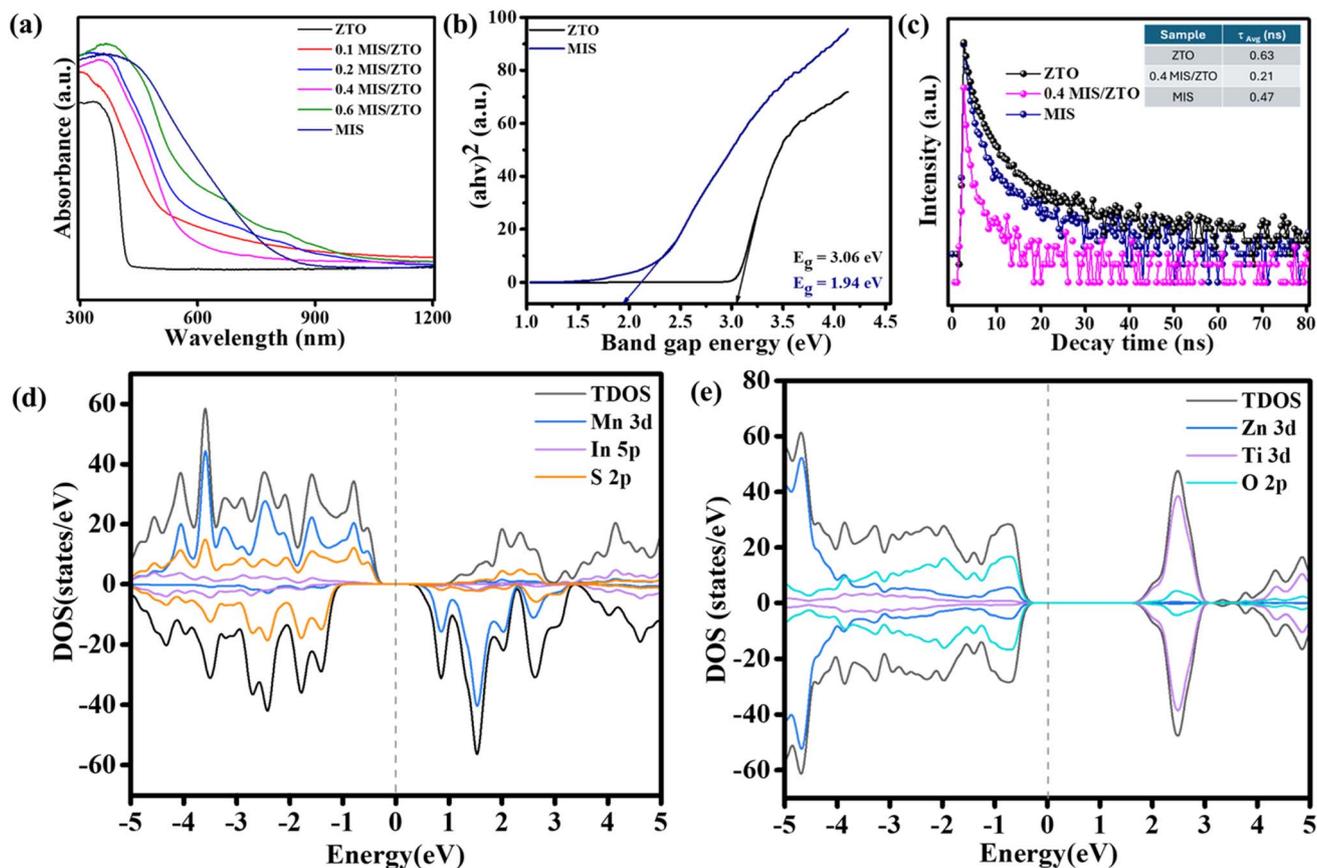*J. Mater. Chem. A*, 2026, **14**, 16409–16423 | **16413**

Fig. 4 (a) Ultraviolet-visible diffuse reflectance spectra of ZTO, MIS, and the MIS/ZTO heterostructures; (b) Tauc plots of ZTO and MIS; (c) photoluminescence decay curves of ZTO, MIS, and the 0.4-MIS/ZTO heterostructure; and the density of states of (d) MIS and (e) ZTO.

$$I(t) = I_{\circ} + B_1 \exp^{-t/\tau_1} + B_2 \exp^{-t/\tau_2} \tag{1}$$

$$\tau_{av} = \frac{B_1 \tau_1^2 + B_2 \tau_2^2}{B_1 \tau_1 + B_2 \tau_2} \tag{2}$$

where τ_{av} represents the average emission lifetime, τ_1 and τ_2 denote the fluorescence lifetimes, and B_1 and B_2 correspond to amplitudes.[37,38] $I(t)$ represent the PL intensity.

The calculated average lifetimes of ZTO, MIS, and 0.4-MIS/ZTO heterostructures were 0.63, 0.47, and 0.21 ns, respectively. These results confirm the rapid charge transfer on the surface of the 0.4-MIS/ZTO heterostructure, which can enhance its photocatalytic performance. The electronic band structures and corresponding density of states (DOS) of the MIS and ZTO systems are examined systematically using DFT calculations to clarify their electronic configurations and orbital interactions. Fig. S2(a) shows that the MIS system exhibits a direct band gap of ~1.515 eV, indicating favorable photon absorption within the visible-light spectrum. In the ZTO component (Fig. 4(e)), the CB was governed by Ti 3d orbitals, whereas the VB was largely contributed by O 2p states, which was consistent with the characteristic electronic configuration of perovskite-type titanates. The calculated band gap of 2.193 eV (Fig. S2(b)) was relatively smaller than the experimentally reported value. The slight deviation of the bandgap observed in this study can be attributed to the intrinsic limitations of DFT.[39–41] In addition,

the orbital-resolved DOS analysis indicated that, in the MIS system, the Mn 3d and S 2p orbitals played a pivotal role in defining the VB maximum while the CB minimum originated from the hybridization between Mn 3d, S 2p, and In 5p orbitals. This strong inter-orbital coupling effectively narrowed the band gap and broadened the visible-light absorption range, enhancing photoinduced charge separation and generating a greater number of surface-active sites. Consequently, these synergistic electronic features substantially improved the photocatalytic efficiency of the MIS/ZTO heterostructure by promoting carrier mobility and interfacial charge transfer dynamics.

3.4 Photoelectrochemical measurements

In the context of the photocatalytic CO_2 reduction, investigating photogenerated charge-carrier dynamics *via* photoelectrochemical analysis is a fundamental step toward clarifying the effect of charge-separation efficiency, interfacial charge transfer, and charge transport kinetics on overall photocatalytic performance.[42–45] The photocurrent responses of the synthesized catalysts under intermittent light irradiation are shown in Fig. 5(a). The 0.4-MIS/ZTO composite exhibited the highest photocurrent intensity of 14.5 μA cm^{-2}, and the other composite samples demonstrated significantly enhanced

16414 | *J. Mater. Chem. A*, 2026, **14**, 16409–16423
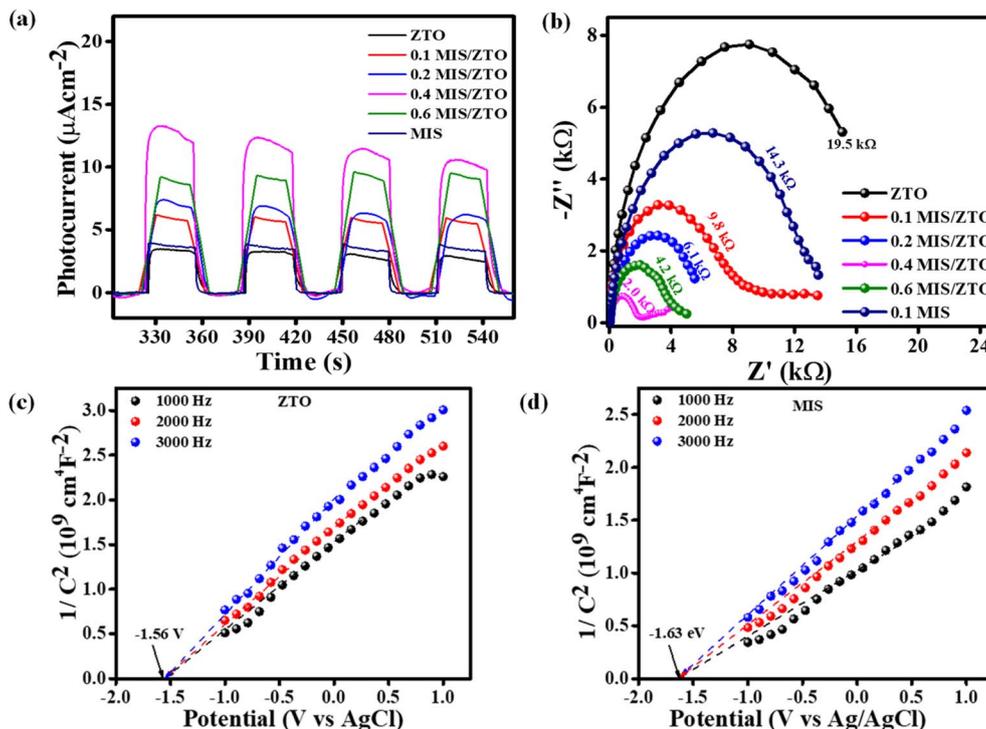
This journal is © The Royal Society of Chemistry 2026

Fig. 5 (a) Transient photocurrent responses and (b) Nyquist plots of ZTO, MIS, and the MIS/ZTO heterostructures. Mott–Schottky curves of (c) ZTO and (d) MIS.

photocurrent responses compared to pristine ZTO and MIS. This enhancement confirmed that the composite structure effectively facilitates charge-carrier migration and suppresses charge recombination. The charge-transfer characteristics are examined *via* electrochemical impedance spectroscopy. Fig. 5(b) shows that the arc radius of 0.4-MIS/ZTO is 2 kΩ, which is smaller than those of MIS (14.3 kΩ) and ZTO (19.5 kΩ), indicating a reduction in charge-transfer resistance. These results confirm that composite photocatalysts exhibit superior charge separation and enhanced photocatalytic efficiency.

M–S plots are analyzed to determine the E_{fb} values of ZTO and MIS, which are −1.56 V (*vs.* Ag/AgCl) and −1.63 V (*vs.* Ag/AgCl), respectively, as shown in Fig. 5(c) and (d), respectively. The positive slopes of the M–S curves confirm that both materials function as n-type semiconductors.[46,47] In addition, as shown in Fig. 4(c) and (d), the VB energy maximum (VBM) positions of MIS and ZTO are 1.02 and 2.46 eV, as shown in Fig. S3. The corresponding potentials *vs.* NHE at pH = 0 are 1.08 and 2.52 V, respectively. Using the bandgap values derived from Tauc plots and applying the fundamental equation $E_g = E_{VB} - E_{CB}$, the CB potentials for MIS and ZTO were −0.86 V (*vs.* NHE) and −0.54 V (*vs.* NHE), respectively.

3.5 Charge transfer mechanism

XPS was used to analyze the electron migration behavior and chemical states of the elements. Fig. 6(a–f) show that Zn, Ti, O, Mn, In, and S are detected. As shown in Fig. 6(b), the Zn 2p XPS curve of ZTO exhibits two characteristic peaks at 1021.77 and 1044.83 eV, which corresponds to Zn $2p_{3/2}$ and Zn $2p_{1/2}$ of Zn^{2+},

respectively.[45,48] Similarly, the Ti 2p XPS curve of ZTO (Fig. 6(c)) shows peaks at 457.66 and 463.47 eV, which corresponds to Ti $2p_{3/2}$ and Ti $2p_{1/2}$ of Ti^{4+}, respectively.[49,50] For pristine MIS, the Mn 2p XPS curve (Fig. 6(d)) shows two peaks at 642.56 and 653.68 eV, which corresponds to Mn $2p_{3/2}$ and Mn $2p_{1/2}$ of Mn^{2+}, respectively.[51] In addition, the high-resolution In 3d XPS curve (Fig. 6(e)) is deconvoluted into two major doublets at 446.58 and 446.22 eV, which corresponds to In $3d_{5/2}$, and at 446.28 and 453.82 eV, which corresponds to In $3d_{3/2}$. The curve indicates the presence of In^{3+}.[52,53] The high-resolution S 2p XPS curve (Fig. 6(f)) shows two peaks at 161.68 and 163.15 eV in pristine MIS, which corresponds to S $2p_{3/2}$ and S $2p_{1/2}$ of S^{2-}, respectively.[54] The binding energies of Mn 2p, In 3d, and S 2p peaks increased on coupling MIS with ZTO, while those of Zn 2p and Ti 2p peaks decreased under the same conditions. As shown in Fig. 6(b–f), the binding energies of all elements shift in the opposite direction under light illumination. In addition, the change in binding energy under both dark and light illumination confirms that the *in situ* growth strategy of MIS/ZTO can create stronger heterogeneous interfaces, which is advantageous for exposing more active sites responsible for CO_2 adsorption.

DFT calculations were utilized to evaluate the work functions of photocatalysts MIS and ZTO for highlighting the interfacial charge-transfer dynamics. Fig. 7 shows that the photocatalyst MIS demonstrates a lower work function (Φ = 4.76 eV) compared with that of photocatalyst ZTO (Φ = 5.21 eV), which implies that MIS has a higher Fermi level compared to that of ZTO. When these semiconductors are brought into contact,

This journal is © The Royal Society of Chemistry 2026

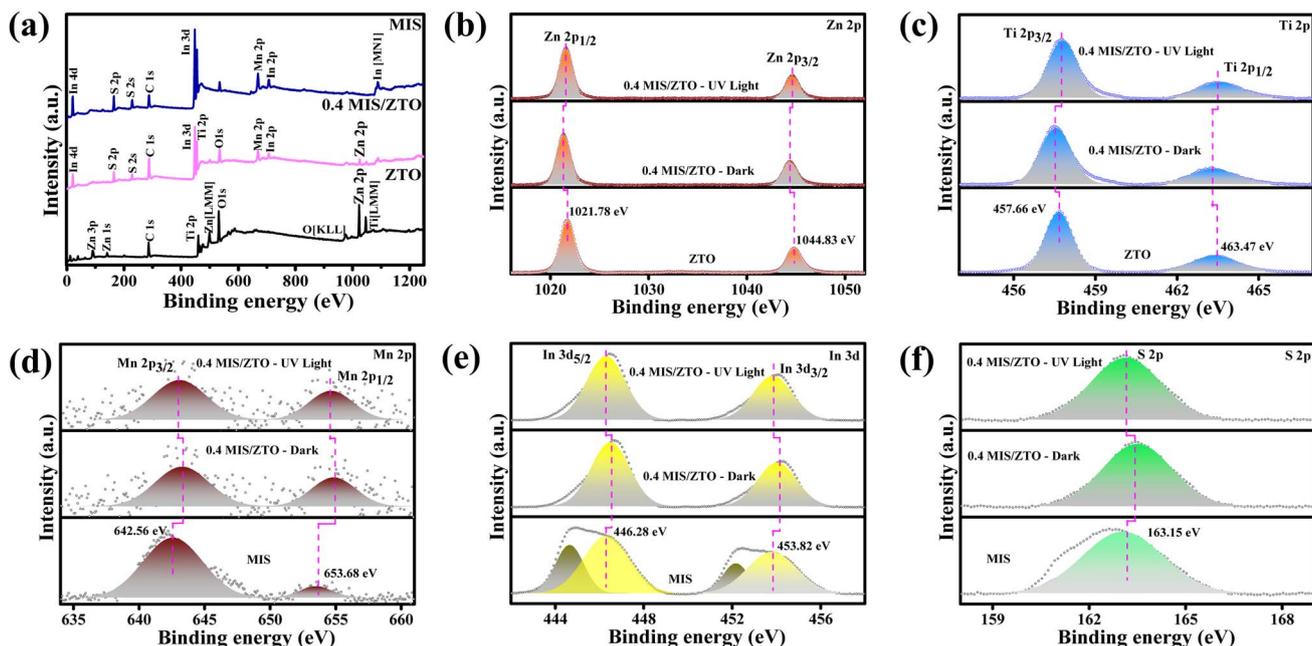*J. Mater. Chem. A*, 2026, **14**, 16409–16423 | **16415**

Fig. 6 (a) XPS survey spectra of ZTO, MIS, and the 0.4-MIS/ZTO heterostructure. High-resolution XPS curves of (b) Zn 2p, (c) Ti 2p, (d) Mn 2p, (e) In 3d, and (f) S 2p.
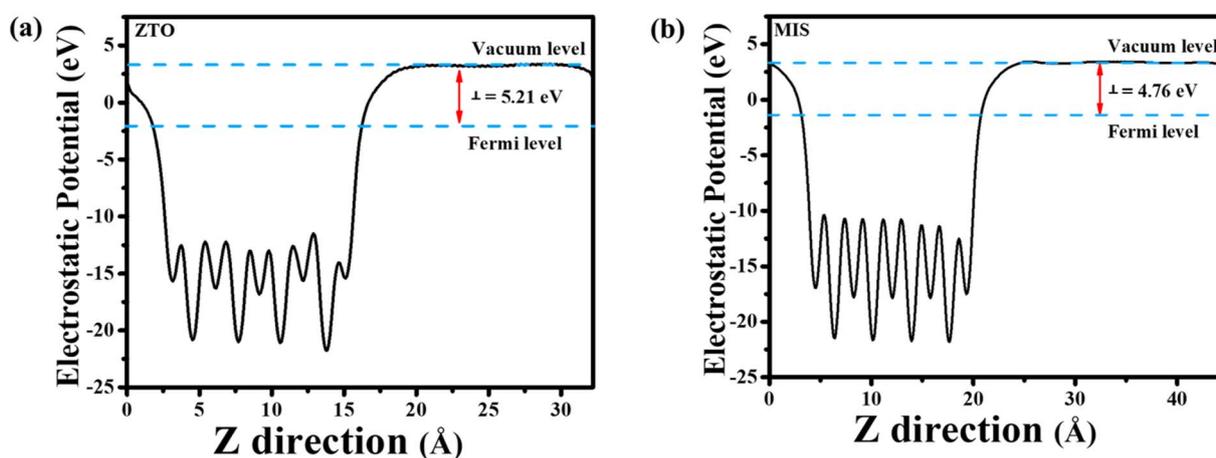

Fig. 7 Electrostatic potentials of (a) ZTO and (b) MIS.

electrons naturally migrate from MIS, with its higher Fermi level and lower work function, to ZTO, which has a lower Fermi level and higher work function until the equilibrium of the Fermi levels is reached. This electron movement results in the accumulation of electrons in ZTO and the depletion in MIS, establishing an interfacial electric field directed from MIS to ZTO. Consequently, this leads to upward band bending in MIS and downward band bending in ZTO near the interface. On illumination, both materials generate electron–hole pairs through excitation from VB to CB. The interface electric field aids in migrating photogenerated electrons from ZTO to MIS and photogenerated holes from MIS to ZTO, which enhances charge separation and minimizes recombination.

Based on the relative positions of the band edges of the two catalysts, the interfacial charge-transfer process adheres to an S-scheme pathway where high-energy electrons in the CB of MIS are preserved and the photogenerated holes in the VB of ZTO are retained. This facilitates the spatially selective recombination of low-energy carriers at the interface.

3.6 Photocatalytic performance

Photocatalytic performances of the ZTO, MIS, and MIS/ZTO photocatalysts were evaluated systematically under UV-vis light irradiation. In this study, 2.0 mg of each photocatalyst was deposited onto an FTO substrate *via* spin coating and positioned horizontally in a custom-made reactor (Fig. S4)

16416 | *J. Mater. Chem. A*, 2026, **14**, 16409–16423

This journal is © The Royal Society of Chemistry 2026

containing H_2O and TEOA. The primary reaction products were H_2, CO, CH_4, and CH_3OH in the liquid phase.

As shown in Fig. 8(a) and (b), pristine ZTO exhibits minimal photocatalytic activity under light irradiation. This limited performance can be attributed to its wide bandgap, which restricts its ability to absorb incident light. The measured average yields of H_2, CO, CH_4, and CH_3OH were 79, 62, 106, and 574 $\mu mol\ g^{-1}$, respectively. For the MIS/ZTO heterostructure photocatalysts, the rate of CO_2 reduction increased initially with increasing MIS loading but decreased beyond an optimal threshold. Among all tested samples, the 0.4-MIS/ZTO heterostructure exhibited the highest photocatalytic yields of CO (484 $\mu mol\ g^{-1}$), CH_4 (345 $\mu mol\ g^{-1}$), and CH_3OH (4457 $\mu mol\ g^{-1}$), as shown in Fig. 8(a) and (b), as well as in the time evolution CO_2 photoreduction presented in Fig. S5 and S6. The detected H_2 in the CO_2 photoreduction originates from the competitive proton reduction reaction, wherein photogenerated electrons reduce protons derived from water in the reaction medium.[55,56] The comparatively lower H_2 evolution (252 $\mu mol\ g^{-1}$) observed for the 0.4-MIS/ZTO heterojunction, as opposed to carbon containing product (CO, CH_4 and CH_3OH), can be attributed to improved charge separation and preferential electron transfer toward adsorbed CO_2 species rather than free protons. The formation of the heterojunction enhances interfacial charge migration and increases the surface electron density at CO_2 adsorption sites, thereby promoting CO_2 activation and multi-electron carbon reduction pathways. This enhanced catalytic performance indicates that the 0.4-MIS/ZTO composite is the most efficient system for driving CO_2 photoreduction reactions. Furthermore, an analysis of CO_2 selectivity revealed that the 0.4-MIS/ZTO photocatalyst exhibited the highest selectivity of 88.12%, outperforming other samples, including pristine ZTO (86.00%), 0.1-MIS/ZTO (82.48%), 0.2-MIS/ZTO (87.10%), 0.6-MIS/ZTO (85.30%), and pristine MIS (78.58%), as shown in Fig. S5.

Beyond the optimal MIS loading, photocatalytic reduction efficiency decreased because of the excessive deposition of MIS on the active surface of ZTO. This hinders light absorption and
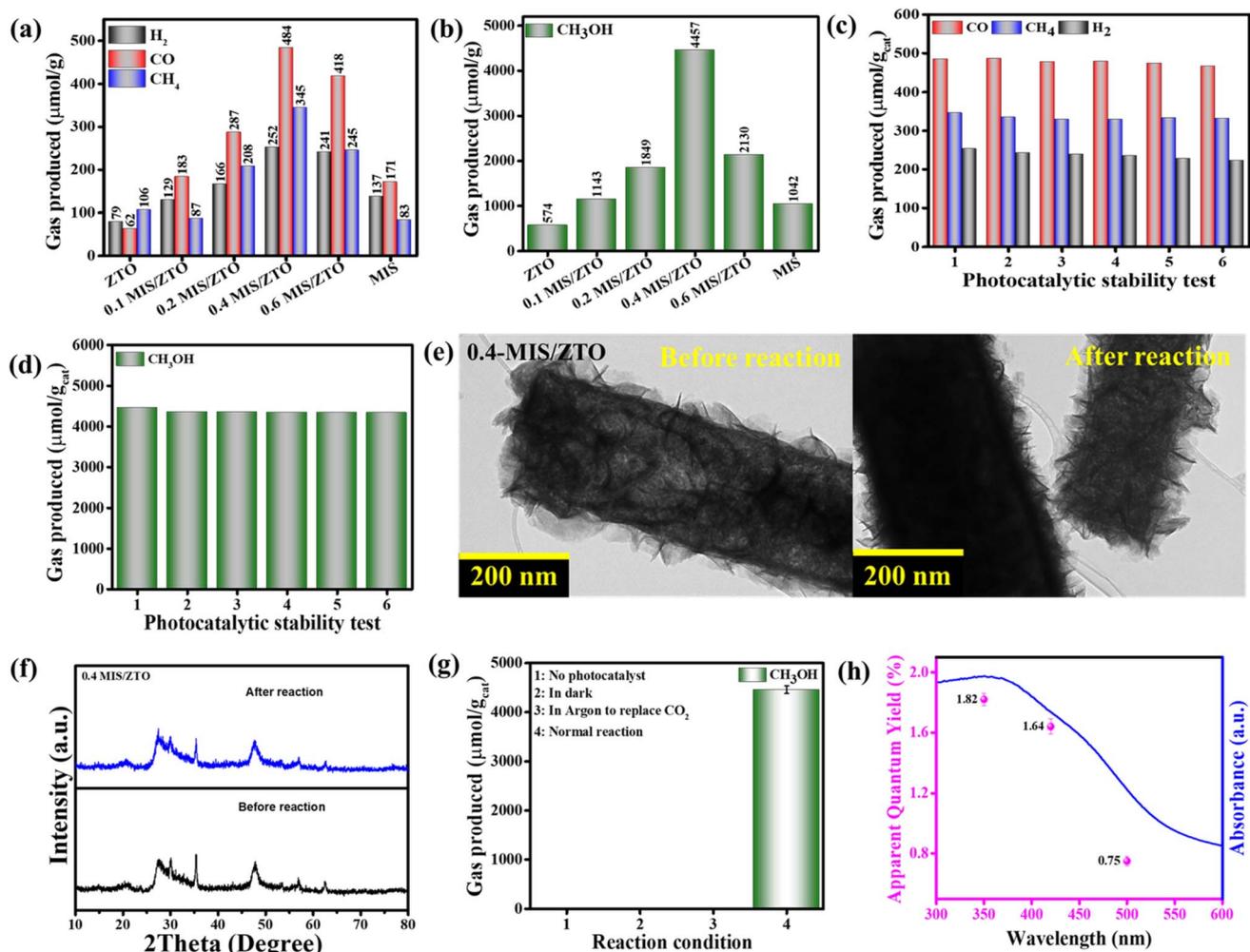

Fig. 8 Products of the photocatalytic reduction of CO_2 over ZTO, MIS, and the MIS/ZTO heterostructures: (a) H_2, CO, and CH_4 and (b) CH_3OH; (c and d) six successive cycles of CO_2 photoreduction over the 0.4-MIS/ZTO heterostructure; (e) experimental conditions for CO_2 photoreduction; (e) TEM and (f) XRD analysis before and after photocatalytic reaction; (g) control experiments for CO_2 photoreduction; (h) AQY of MIS/ZTO and light absorption spectra.

reduces the overall photocatalytic performance.[52,57,58] The stability of the photocatalyst was evaluated through recycling experiments, demonstrating that 0.4-MIS/ZTO remained stable up to six cycles of CO_2 reduction, as shown in Fig. 8(c and d). As evidenced by TEM and XRD analyses (Fig. 8(e and f)), the 0.4-MIS/ZTO heterostructured photocatalyst exhibits no discernible structural degradation, indicating excellent structural stability. Considering the number of photogenerated charge carriers that actively participated in the CO_2 photoreduction process, the 0.4-MIS/ZTO composite exhibited significantly enhanced photoconversion efficiency, achieving CH_4 and CH_3OH yields that were 3.2 and 7.7 times higher, respectively, than those obtained with pristine ZTO. The behaviors of optimal MIS/ZTO heterostructures during the photocatalytic CO_2 reduction tests under the selected experimental conditions are summarized in Fig. 8(g), where the highest CH_3OH yield was 4457 µmol g^{-1} under normal reaction conditions. The apparent quantum yields (AQY) of the optimized MIS/ZTO at wavelengths of 350, 420, and 500 nm, are determined to be 1.82, 1.64, and 0.75% respectively, shown in Fig. 8(h), as its procedure is described in SI Section (S3). Furthermore, we quantified product selectivity and accounted for the carbon balance based on the evolved yield of CO, CH_4, and CH_3OH, as illustrated in Fig. S7 and Table S1. In particular, the observed CH_3OH yield for the 0.4-MIS/ZTO photocatalyst is competitive with those of representative titanate-based photocatalysts reported in the literature (Table S2). Generally, the results indicate that the 0.4-MIS/ZTO heterojunction performs favorably among reported titanate-based systems, demonstrating its potential as an efficient platform for photocatalytic CO_2 reduction.

3.7 Photocatalytic mechanism

DRIFTS was employed to investigate the surface-reactive intermediates and clarify the mechanistic pathway of CO_2 activation and reduction (CO_2RR) over the MIS/ZTO heterostructures. The 0.4 MIS/ZTO system (Fig. 9(a)) exhibits distinct absorption bands at 1548,[59] 1412,[60] and 1028 cm^{-1},[59] which are attributed to bridging carbonate (b-CO_3^{2-}), monodentate carbonate (m-CO_3^{2-}), and bicarbonate (HCO_3^-) species, respectively. In addition, the weak band centered at 1236 cm^{-1} (ref. 61) corresponds to physically adsorbed CO_2 molecules retained on the catalyst surface. The emergence of a peak near 1711 cm^{-1},[62]
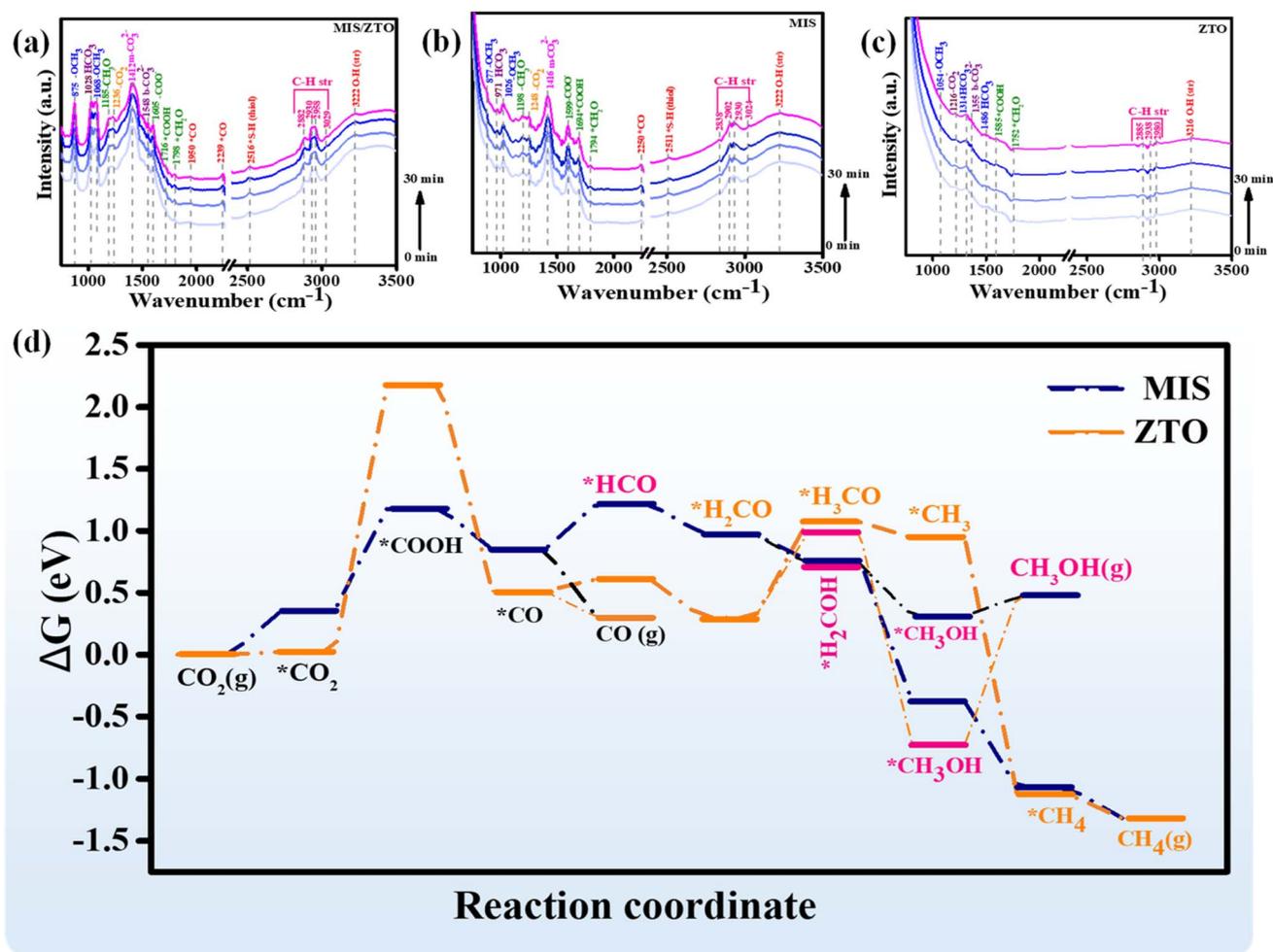

Fig. 9 *In situ* Fourier transform infrared (FT-IR) spectra of (a) 0.4-MIS/ZTO, (b). MIS, (c) ZTO and (d) calculated Gibbs free energy profiles for products evolution pathways.

16418 | *J. Mater. Chem. A*, 2026, **14**, 16409–16423

This journal is © The Royal Society of Chemistry 2026

attributed to the carboxylate intermediate (*COOH), confirms the partial reduction and deoxygenation of CO_2 occurring at the heterointerface. This is a critical step preceding C–O bond cleavage. The observation of CO-related vibrational modes at 1950 and 2239 cm^{-1} (ref. 63) indicates the generation and subsequent desorption of CO, which corroborates its role as a key reduction product in the present CO_2RR system. The appearance of a band at 1798 cm^{-1}, corresponding to the formaldehyde-like (*CH_2O) intermediate, suggests the further hydrogenation of CO species toward CH_4 formation, which is consistent with the observed product distribution. In the lower wavenumber region (875–1068 cm^{-1}),[64] the enhanced intensity of bands related to bicarbonate (HCO_3^-) and methoxy (OCH_3) species implies facile transformation into methanol (CH_3OH) through stepwise hydrogenation reactions. These IR spectral features are indicative of crucial CO_2-derived adsorbed intermediates, which suggests that the atomic-scale active sites of 0.4 MIS/ZTO facilitate effective CO_2 adsorption (Fig. S8), which is a fundamental prerequisite for photocatalytic CO_2 reduction.

In contrast, significantly weaker DRIFTS signals are detected for the individual MIS and ZTO samples (Fig. 9(b and c)). For pristine MIS, the presence of vibrational features at 1416 cm^{-1} (m-CO_3^{2-}), 971 cm^{-1} (HCO_3^-), 1694 cm^{-1} (*COOH), and 1198 cm^{-1} (CH_3O) confirms limited CO_2 adsorption and activation capability. Meanwhile, ZTO exhibits relatively weak peaks at 1355 cm^{-1} (b-CO_3^{2-}), 1585 cm^{-1} (*COOH), and 1752 cm^{-1} (CH_2O), indicating incomplete charge transfer and insufficient surface reduction activity.

In summary, DRIFTS results demonstrate that the MIS/ZTO provides abundant active sites that promote synergistic CO_2 adsorption, activation, and multielectron transfer, markedly enhancing CO_2RR performance. The CO_2RR activity of the integrated MIS/ZTO heterojunction surpasses that of the individual MIS or ZTO components, affirming the decisive role of heterointerface engineering in facilitating efficient charge migration and stabilizing key intermediates during CO_2 photoreduction.

The DFT calculations provide insights into the reaction network that facilitates CO_2 photoreduction over ZTO and MIS photocatalysts. This network reveals two distinct electron-transfer pathways: one-electron pathway, where electrons are transferred sequentially at each elementary step, and two-electron pathway, characterized by the simultaneous introduction of two electrons as shown in Fig. 9(d). Based on the proposed CO_2RR pathways, Gibbs free energy profiles were evaluated systematically on the surfaces of MIS and ZTO. The reaction sequence begins with CO_2 adsorption (*CO_2), followed by stepwise proton–electron transfer to form *COOH and subsequently *CO, which desorbs as CO(g).[65] Further hydrogenation of *CO can proceed through *HCO, *H_2CO, and *H_2COH intermediates to yield CH_3OH, or alternatively through *H_3CO and *CH_3 toward CH_4 formation. These elementary steps collectively describe the multielectron processes leading to CO, CH_3OH, and CH_4 as final products.

The Gibbs free energy analysis highlights pronounced differences between the two catalytic components of the MIS/ZTO heterostructure. For the initial CO_2(g) → *CO/CO(g)

pathway, the theoretical overpotential determined by the rate-determining step on MIS is limited to 0.826 V, while ZTO requires a considerably higher theoretical overpotential of 2.156 V. During the subsequent hydrogenation of *CO toward CH_3OH(g), MIS exhibits only a small additional Gibbs free energy requirement of 0.373 eV, while ZTO encounters two thermodynamically unfavorable steps with the maximum Gibbs free energy change reaching 1.190 eV. In the CH_4 formation pathway, the transformation from *HCO proceeds spontaneously on MIS, as evidenced by a negative Gibbs free energy change, while ZTO requires an extra 0.772 eV to drive the reaction forward. These results demonstrate that MIS provides a more favourable energetic landscape for CO_2 activation and its subsequent reduction to CH_3OH as summarized in Fig. S9. Therefore, the formation of CO and CH_3OH shares a common initial pathway through H_2CO as a key intermediate, with the ultimate product selectivity being determined by the subsequent transformation of this crucial intermediate. Consistent with this mechanistic picture, the MIS/ZTO heterostructure exhibits enhanced experimental yields of CO, CH_3OH, and CH_4, which suggests that the strong reduction capability of MIS promotes CO_2 activation and facilitates multiple reduction pathways.

The electronic structure of the MIS/ZTO heterostructure was systematically investigated at three key stages (prior to contact, after interface formation, and under light irradiation) to identify the interfacial charge-transfer mechanism underlying the enhanced CO_2 photoreduction performance. This analysis, summarized in Fig. 10(a), provides insight into how interfacial interactions and photoexcitation jointly promote improved CO_2 reduction activity. As illustrated in Fig. 10(b), the interfacial region is defined as the area between the black and blue dashed lines. The one-dimensional charge-density difference along the z direction reveals pronounced charge redistribution upon heterojunction formation. Electrons preferentially migrate from the MIS layer toward the ZTO side. This trend is corroborated by the three-dimensional isosurface of the electron-density difference shown in Fig. 10(c), which clearly visualizes producing an electron-rich region in ZTO and a corresponding depletion region in the MIS region near the interface. This interfacial charge redistribution generates a built-in electric field oriented from MIS to ZTO, which agrees with the above XPS results. Under light irradiation, the band bending-induced internal electric field (IEF) governs the migration and recombination behavior of photoexcited charge carriers.[66,67] Consequently, the photogenerated electrons in the CB of ZTO are driven to recombine with holes in the VB of MIS, confirming the establishment of an S-scheme heterostructure between the two components.

The established IEF not only facilitates directional charge separation and suppresses carrier recombination but also provides the electrostatic basis for the S-scheme charge-transfer pathway across the interface. Further insight into the interfacial interaction is obtained from the electron localization function (ELF) shown in Fig. 10(d). These results reveal a distinct accumulation of localized electron density at the interface. This suggests that, while the heterojunction is stabilized by van der
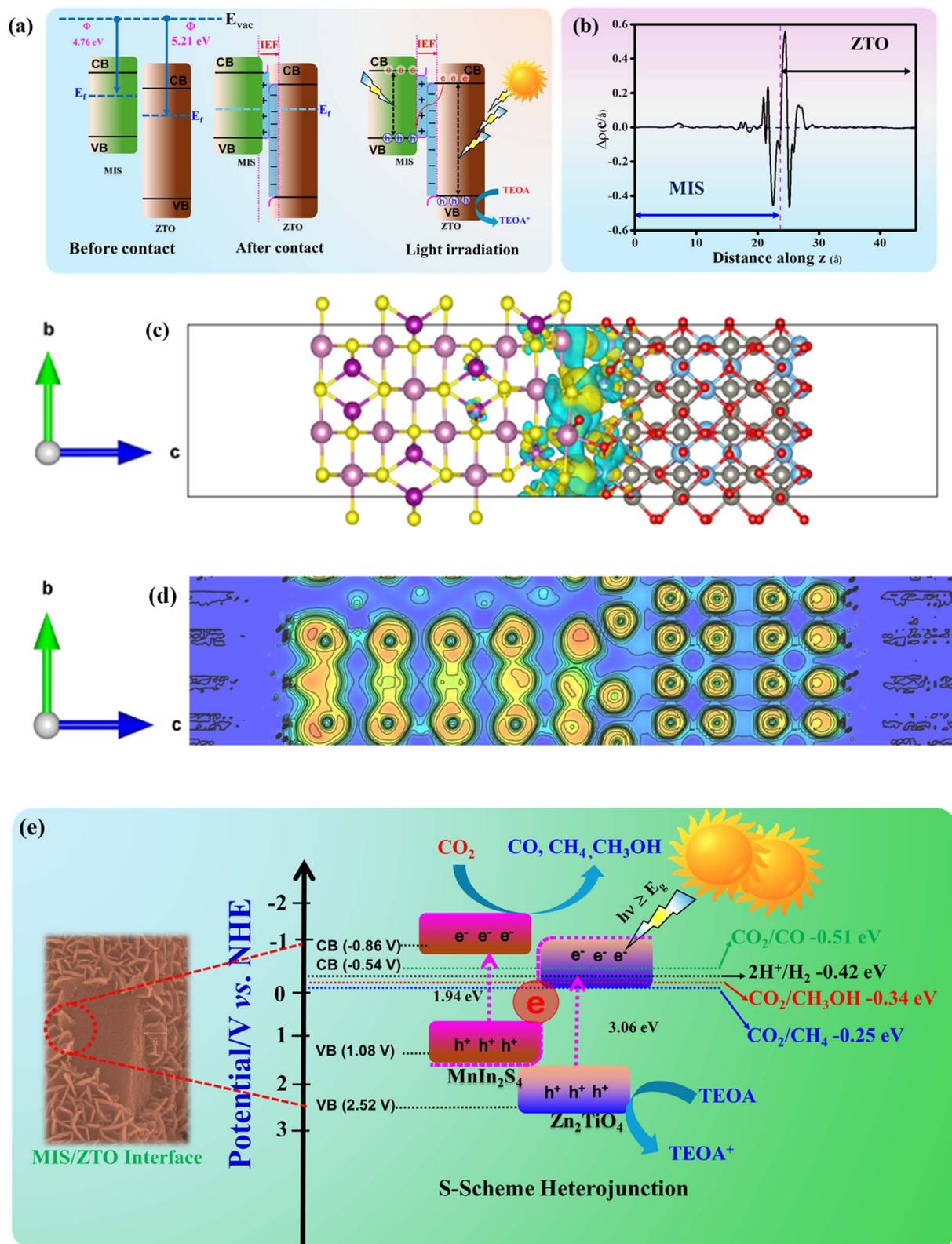
This journal is © The Royal Society of Chemistry 2026

J. Mater. Chem. A, 2026, **14**, 16409–16423 | **16419**

Fig. 10 (a) Formation mechanism of S-scheme heterojunction in MIS/ZTO, (b) plane-integrated electron density difference along the *z* direction for the MIS/ZTO heterojunction, (c) 3D isosurface of the electron density difference of the MIS/ZTO heterojunction, (d) the electron local function of MIS/ZTO heterojunction, (e) schematic of the mechanism of the photocatalytic reduction of CO$_2$ over the MIS/ZTO heterojunction under UV-vis irradiation.

16420 | *J. Mater. Chem. A*, 2026, **14**, 16409–16423

This journal is © The Royal Society of Chemistry 2026

Waals interactions, partial covalent bonding characteristics also emerge.[68]

A schematic of the mechanism of the photocatalytic reduction of CO_2 is shown in Fig. 10(e). The complementary VB revealed that ZTO has a higher VB potential than that of MIS (2.52 V compared with 1.08 V), thereby suggesting a deeper VB position. This electronic configuration, along with bandgaps of 1.94 eV for MIS and 3.06 eV for ZTO, confirms that the MIS system has a greater reduction capability than that of ZTO. Upon light irradiation, electrons and holes are excited on ZTO and MIS. Some of the photogenerated electrons in the CB of ZTO migrate to VB of MIS because of the effect of the built-in interfacial electric field, thereby facilitating effective charge separation within the S-scheme heterojunction.[51,69] This charge-transfer pathway enables high-energy electrons to accumulate in the CB of MIS, which then convert CO_2 into CO, CH_4, CH_3OH, and other intermediate products. The TEOA acts as a hole scavenger,[8,70,71] consuming holes in the VB of ZTO and suppressing charge recombination. The S-scheme charge-transfer mechanism plays a crucial role in optimizing the charge-separation efficiency and enhancing the overall performance of the photocatalytic reduction of CO_2.

4   Conclusion

In this study, a ZTO photocatalyst was synthesized *via* a sol–gel method, and a facile solvothermal approach was employed to deposit MIS nanostructures onto one-dimensional ZTO. This process resulted in the formation of a heterostructured catalyst with enhanced photocatalytic activity for CO_2 reduction. Incorporating MIS significantly improved photocatalytic conversion efficiency, yielding a remarkable production of CO (484 $\mu mol\ g^{-1}$), CH_4 (345 $\mu mol\ g^{-1}$), and CH_3OH (4457 $\mu mol\ g^{-1}$) from the dissolved CO_2. These values correspond to 7.8-, 3.2-, and 7.7-fold enhancements, respectively, compared with pristine ZTO. The superior photocatalytic performance of the MIS/ZTO heterostructure can be attributed to its rationally designed S-scheme charge-transfer mechanism, as confirmed by the XPS and DFT calculations with more active sites residing on MIS moiety. The S-scheme heterojunction not only effectively promotes the spatial separation of photogenerated charge carriers but also provides high reduction potential, facilitating multielectron transfer for the efficient photoreduction of CO_2. This study provides valuable insights into the fabrication and charge-transfer dynamics of heterojunction-based photocatalysts, thereby presenting a promising strategy for enhancing the photocatalytic efficiency of gas–solid CO_2 conversion systems.

Author contributions

Plassidius J. Chengula: conceptualization, methodology, data curation, formal analysis, writing—original draft. Junying Zhang: resources, supervision, validation, writing—review & editing. Hazina Charles: experimentation, data curation, formal analysis, validation. Ji Yeon Seo: experimentation, data curation, formal analysis. Xiaofang Jia: methodology, data curation, formal analysis, writing—review & editing. Caroline S. Lee: resources, funding acquisition, supervision, writing—review and editing.

Conflicts of interest

The authors declare that they have no competing financial interests or personal relationships that may have influenced the work reported in this study.

Data availability

The data supporting this study are provided in the supplementary information (SI). Supplementary information: additional characterization data (SEM, CO_2 adsorption–desorption, XPS valence band spectra), photoelectrochemical measurements, CO_2 photoreduction setup and activities, DFT adsorption geometries and band structures, and the comparison of performances of titanate based photocatalysts. See DOI: https://doi.org/10.1039/d6ta01118g.

Acknowledgements

References

1 L. Huang, S. Mo, X. Zhao, J. Zhou, Y. Zhang, X. Zhou, Y. Fan, Q. Xie and D. Ye, *J. Environ. Chem. Eng.*, 2024, **12**, 112566.

2 Z. Xiao, P. Li, H. Zhang, S. Zhang, X. Tan, F. Ye, J. Gu, J. Zou and D. Wang, *Fuel*, 2024, **362**, 130906.

3 Z. Li, J. Xiong, Y. Huang, Y. Huang, G. I. N. Waterhouse, Z. Wang, Y. Mao, Z. Liang and X. Luo, *Chem.–Eng. J.*, 2024, **486**, 150304.

4 N. Singhal, A. Ali, A. Vorontsov, C. Pendem and U. Kumar, *Appl. Catal., A*, 2016, **523**, 107–117.

5 X. Zhao, Y. Xia, X. Wang, N. Wen, H. Li, X. Jiao and D. Chen, *Chem.–Eng. J.*, 2022, **449**, 137874.

6 M. Li, L. Zhang, X. Fan, Y. Zhou, M. Wu and J. Shi, *J. Mater. Chem. A*, 2015, **3**, 5189–5196.

7 P. J. Chengula, H. Charles, R. C. Pawar and C. S. Lee, *Chemosphere*, 2024, **351**, 141197.

8 H. Charles, R. C. Pawar, H. Khan, P. J. Chengula and C. S. Lee, *J. Environ. Chem. Eng.*, 2023, **11**, 109917.

9 J. Ding, X. Liu, M. Shi, T. Li, M. Xia, X. Du, R. Shang, H. Gu and Q. Zhong, *Sol. Energy Mater. Sol. Cells*, 2019, **195**, 34–42.

10 W. Zhang, J. Zhao, A. A. Allam, Y. Xin, J. Lin, T. Gao, J. S. Ajarem, X. Li, C. Wang and D. W. Bahnemann, *Energy Fuels*, 2022, **36**, 13852–13862.

This journal is © The Royal Society of Chemistry 2026

J. Mater. Chem. A, 2026, **14**, 16409–16423 | **16421**

11 P. Chen, H. Liu, W. Cui, S. C. Lee, L. Wang and F. Dong, *EcoMat*, 2020, **2**, 1–31.

12 Q. D. Truong, H. T. Hoa, D. V. N. Vo and T. S. Le, *New J. Chem.*, 2017, **41**, 5660–5668.

13 W. F. Tan, Y. T. Yu, M. X. Wang, F. Liu and L. K. Koopal, *Cryst. Growth Des.*, 2014, **14**, 157–164.

14 Q. Fu and L. Guo, *AIP Adv.*, 2022, **12**, 15201.

15 S. A. Mayén-Hernández, G. Torres-Delgado, R. Castanedo-Pérez, M. G. Villarreal, A. Cruz-Orea, J. G. M. Alvarez and O. Zelaya-Angel, *J. Mater. Sci.: Mater. Electron.*, 2007, **18**, 1127–1130.

16 H. Cheng, J. Wu, F. Tian, Q. Liu, X. Qi, Q. Li, W. Pan, Z. Li and J. Wei, *Chem.–Eng. J.*, 2019, **360**, 951–963.

17 G. Tan, L. Zhang, S. Wei, A. Xia and H. Ren, *Cryst. Res. Technol.*, 2012, **47**, 1279–1283.

18 M. Yu, Q. Pu, X. Liao, H. Yu, S. Lin, Z. Li, C. Yu, H. Wang and X. Zhong, *J. Mater. Sci.: Mater. Electron.*, 2021, **32**, 17848–17864.

19 M. Wu, Y. Zhang, W. Szeto, W. Pan, H. Huang and D. Y. C. Leung, *Chem. Eng. Sci.*, 2019, **200**, 203–213.

20 Z. P. Tshabalala, J. Kano, H. C. Swart and D. E. Motaung, *Phys. B*, 2024, **676**, 415687.

21 Y. Qu, W. Zhou and H. Fu, *ChemCatChem*, 2014, **6**, 265–270.

22 A. P. Souri, N. Andrigiannaki, M. Moschogiannaki, V. Faka, G. Kiriakidis, A. Malankowska, A. Zaleska-Medynska and V. Binas, *Appl. Sci.*, 2021, **11**, 1–14.

23 Y. W. Wang, P. H. Yuan, C. M. Fan, Y. Wang, G. Y. Ding and Y. F. Wang, *Ceram. Int.*, 2012, **38**, 4173–4180.

24 J. Peng, Y. Wang, J. Bai, D. Ma, R. Zhao, J. Han and L. Wang, *Fuel*, 2022, **325**, 124937.

25 S. Ke, X. Cheng, Q. Wang, Y. Wang and Z. Pan, *Ceram. Int.*, 2014, **40**, 8891–8895.

26 B. Ding, K. Zuo, L. Zhang, S. Liu, S. Zheng, L. Mao and J. Zhang, *J. Environ. Chem. Eng.*, 2024, **12**, 114594.

27 Q. Chen, L. Wu, X. Zhao and X. J. Yang, *J. Mol. Liq.*, 2022, **353**, 1–9.

28 J. Zhao, D. Zhou, Q. He, J. Zhang and B. Yao, *J. Alloys Compd.*, 2025, **1010**, 177300.

29 L. Wang, X. Fu, C. Zhu, X. Xiao, Y. Xu, W. Huang, Z. He, Y. Xia, T. Yang and Y. Gao, *Sep. Purif. Technol.*, 2025, **355**, 129712.

30 G. Kresse and J. Furthmüller, *Phys. Rev. B: Condens. Matter Mater. Phys.*, 1996, **54**, 11169–11186.

31 G. Kresse and D. Joubert, *Phys. Rev. B: Condens. Matter Mater. Phys.*, 1999, **59**, 1758–1775.

32 S. Grimme, J. Antony, S. Ehrlich and H. Krieg, *J. Chem. Phys.*, 2010, **132**, 154104.

33 J. K. Nørskov, J. Rossmeisl, A. Logadottir, L. Lindqvist, J. R. Kitchin, T. Bligaard and H. Jónsson, *J. Phys. Chem. B*, 2004, **108**, 17886–17892.

34 Z. Ye, X. Xiao, J. Chen and Y. Wang, *J. Photochem. Photobiol., A*, 2019, **368**, 153–161.

35 W.-Y. Chen, C.-P. Wang, P.-C. Chen, K.-Y. A. Lin, S. Ghosh, C.-W. Huang and V.-H. Nguyen, *Catalysts*, 2021, **11**, 854.

36 J. Klein, L. Kampermann, B. Mockenhaupt, M. Behrens, J. Strunk and G. Bacher, *Adv. Funct. Mater.*, 2023, **33**, 2304523.

37 P. Anand, A. Verma, Y. A. Hong, A. Hu, D. P. Jaihindh, M. S. Wong and Y. P. Fu, *Chemosphere*, 2023, **310**, 136847.

38 H. Deng, X. Fei, Y. Yang, J. Fan, J. Yu, B. Cheng and L. Zhang, *Chem.–Eng. J.*, 2021, **409**, 2–11.

39 M. J. Lucero, T. M. Henderson and G. E. Scuseria, *J. Phys.: Condens. Matter*, 2012, **24**, 145504.

40 B. G. Janesko, T. M. Henderson and G. E. Scuseria, *Phys. Chem. Chem. Phys.*, 2009, **11**, 443–454.

41 F. Viñes, O. Lamiel-García, K. Chul Ko, J. Yong Lee and F. Illas, *J. Comput. Chem.*, 2017, **38**, 781–789.

42 X. Yuan, D. Shen, Q. Zhang, H. Zou, Z. Liu and F. Peng, *Chem.–Eng. J.*, 2019, **369**, 292–301.

43 M. Huang, Y. Chu, B. Xi, N. Shi, B. Duan, C. Zhang, W. Chen, J. Feng and S. Xiong, *Small*, 2020, **16**, 1–12.

44 Z. Ni, Y. Shen, L. H. Xu, G. Xiang, M. Chen, N. Shen, K. Li and K. Ni, *Appl. Surf. Sci.*, 2022, **576**, 151868.

45 R. Sasikala, M. Kandasamy, V. Ragavendran, S. Suresh, V. Sasirekha, S. Murugesan, S. Sagadevan and J. Mayandi, *Phys. B*, 2022, **646**, 414300.

46 H. Razavi-Khosroshahi, S. Mohammadzadeh, M. Hojamberdiev, S. Kitano, M. Yamauchi and M. Fuji, *Adv. Powder Technol.*, 2019, **30**, 1290–1296.

47 H. She, Y. Qiao, B. Liu, S. Li, L. Wang, J. Huang and Q. Wang, *Chem. Eng. J.*, 2026, **527**, DOI: 10.1016/j.cej.2025.171741.

48 C. Wattanawikkam and W. Pecharapa, *IEEE Trans. Ultrason. Ferroelectrics Freq. Control*, 2016, **63**, 1663–1667.

49 J. Y. Lee and J.-H. Choi, *Materials*, 2019, **12**, 1265.

50 L. Wang, B. Cheng, L. Zhang and J. Yu, *Small*, 2021, **17**, 1–9.

51 Y. Zhu, D. Wang, M. Ding, T. Yao, M. Liu and W. You, *Appl. Surf. Sci.*, 2022, **582**, 152418.

52 D.-E. Lee, B. M. Abraham, S. Moru, V. Devthade, W.-K. Jo and S. Tonda, *J. Alloys Compd.*, 2024, **1009**, 176881.

53 W. Chen, Z. C. He, G. B. Huang, C. L. Wu, W. F. Chen and X. H. Liu, *Chem.–Eng. J.*, 2019, **359**, 244–253.

54 D. Kanakaraju and A. Chandrasekaran, *Sci. Total Environ.*, 2023, **868**, 161525.

55 X. Zhang, Y. Song, X. Niu, X. Lin, S. Zhong, H. Lin, B. Teng and S. Bai, *Appl. Catal., B*, 2024, **342**, 123445.

56 Y. Liu, A. Deng, Y. Yin, J. Lin, Q. Li, Y. Sun, J. Zhang, S. Li, S. Yang, Y. Xu, H. He, S. Liu and S. Wang, *Appl. Catal., B*, 2025, **362**, 124724.

57 F. Iqbal, A. Mumtaz, S. Shahabuddin, M. I. Abd Mutalib, M. S. Shaharun, T. D. Nguyen, M. R. Khan and B. Abdullah, *J. Chem. Technol. Biotechnol.*, 2020, **95**, 2208–2221.

58 S. S. Wang, X. Liang, Y. K. Lv, Y. Y. Li, R. H. Zhou, H. C. Yao and Z. J. Li, *ACS Appl. Energy Mater.*, 2022, **5**, 1149–1158.

59 C. Luo, J. Zhao, Y. Li, W. Zhao, Y. Zeng and C. Wang, *Appl. Surf. Sci.*, 2018, **447**, 627–635.

60 S. H. Liu, J. S. Lu, Y. C. Pu and H. C. Fan, *J. CO$_2$ Util.*, 2019, **33**, 171–178.

61 Y. Shang, Y. Hou, X. Cao, H. Liu, X. Jin, J. Liu, C. Yan, Y. Qian, L. Song, Z. Qi, P. Song, Y. Zhou, D. Liu, Z. Liu, F. Jing, Q. Yan, G. Chen and C. Lv, *Chem.–Eng. J.*, 2024, **486**, 150306.

62 C. Chen, P. Zhao, Q. Li, Y. Zhang, T. Sun, C. Hu and J. Ma, *Fuel*, 2024, **367**, 131446.

16422 | *J. Mater. Chem. A*, 2026, **14**, 16409–16423

This journal is © The Royal Society of Chemistry 2026

63 Q. Zhu, W. Huang, J. Shen, H. Jiang, Y. Zhu and C. Li, *Chem.– Eng. J.*, 2024, **499**, 156663.

64 M. Ma, Z. Huang, L. Li, W. Zhang, R. Guo, R. Zhang, W. Fa, C. Han, Y. Cao, S. Yu and Y. Zhou, *Appl. Catal., B*, 2023, **330**, 122626.

65 R. Hua, J. Zhao, H. She, L. Wang, J. Huang and Q. Wang, *Chem. Eng. J.*, 2025, **521**, DOI: 10.1016/j.cej.2025.166444.

66 H. Zhao, H. Song, Z. Pan, X. Zhu, D. Ye, Y. Yang, H. Wang, R. Chen and Q. Liao, *ACS Nano*, 2025, **19**, 18661–18673.

67 Z. Meng, J. Zhang, H. Long, H. García, L. Zhang, B. Zhu and J. Yu, *Angew. Chem., Int. Ed. Engl.*, 2025, **64**, e202505456.

68 S. Fan, Q. Yang, G. Yin, X. Qi, Y. Feng, J. Ding, Q. Peng, Y. Qu, Q. Wang, Y. Shen, M. Wang and X. Gong, *Small*, 2024, **20**, 1–9.

69 S. Wang, Z. Zheng, Y. Guan, J. Mei, R. Liu, D. Mao, J. Shen and Z. Li, *Mater. Today Commun.*, 2022, **33**, 104733.

70 R. C. Pawar, P. J. Chengula, H. Khan, H. Charles and C. S. Lee, *Dalton Trans.*, 2023, **52**, 12832–12844.

71 H. Charles, P. J. Chengula, R. C. Pawar, H. Khan, S. Kim and C. S. Lee, *J. Water Process Eng.*, 2023, **56**, 104307.

This journal is © The Royal Society of Chemistry 2026

J. Mater. Chem. A, 2026, **14**, 16409–16423 | **16423**